Engineering grain boundary sliding and cavitation effects in superplastic alloys employing thermodynamics

E. I. Galindo-Nava*[1], G. Torres-Villaseñor[2] and P. E. J. Rivera-Díaz-del-Castillo[1]

Plastic deformation by grain boundary sliding in superplastic alloys is described by a novel thermostatistical approach. The Gibbs free energy for cavity formation at moving grain boundaries is obtained. It equals the competition between the stored energy at the boundaries and the energy dissipated by grain boundary sliding. The latter is approximated by an entropy term induced by moving dislocations to facilitate boundary displacement. Strength loss evolution is estimated from the cavity evolution rate. The theory describes superplastic behaviour of Zn22Al, Zn21Al2Cu and Mg3Al1Zn for various temperatures, strain rates, grain sizes, and specimen geometries. Transition maps are defined for finding the optimal conditions for achieving superplastic behaviour in terms of composition, temperature, geometry and strain rate.

Keywords: Grain boundary sliding, Superplasticity, Cavitation, Dislocations, Alloy design, Themostatistics

Introduction

Superplastic forming can be employed to readily shape alloys without complex processing schedules. Superplastic polycrystalline alloys display high tensile elongations, ranging from 200 up to a few thousand percent before failure at relatively high temperatures.[1] This behaviour is often controlled by grain boundary sliding (GBS),[2,3] where adjacent grains displace with respect to each other to accommodate strain. This process usually occurs in ultra–fine–grain (UFG) materials (with grain sizes of a few microns or less), and at relatively elevated temperatures ($\sim 0{\cdot}5T_m$ and above, with T_m being the melting point).

Two major mechanisms are involved in GBS:[1,2] the first mode is based on the movement of intergranular dislocations, facilitating boundary displacement; the second mode involves grain elongation through stress–directed vacancy diffusion. The former usually takes place at medium temperatures ($T \leq 0{\cdot}6T_m$**), whereas the latter is present above this value.

Meyers *et al.*[3] have pointed out that grain boundary sliding can play a significant role in the development and exhibition of novel properties of UFG and nanostructured materials. Moreover, Van Swygenhoven *et al.*[4,5] have shown that GBS is the primary deformation mechanism in nanocrystalline materials, and that such sliding mechanism results in stress build–up across neighbouring grains. However, the formability of these materials is often limited by their failure due to intergranular cracking.[1,6,7] Crack growth is commonly driven by cavity formation and interlinkage at grain boundaries.

Possible cavitation nucleation mechanisms at grain boundaries are:[8–10]

(i) high stress concentrations by grain boundary sliding (mostly at triple points)
(ii) intergranular slip intersection with grain boundaries and non–deformable second phase particles
(iii) vacancy condensation.

Several modelling approaches at different scales have been proposed to characterise the factors involving grain boundary sliding and cavity evolution. For instance, Qi *et al.*[11] have employed molecular dynamics to describe grain boundary misorientation on sliding; these results were correlated with the grain boundary energy. Kim and Morita[12] theoretically described the sliding rate and the stress distribution on a boundary at the steady state. They described a balance between the relative boundary displacement rate and the grain–boundary diffusion rate. They also have analysed the sliding rate in boundaries containing second–phase particles with various shapes.[13] Khaleel *et al.*[8] studied superplastic deformation and cavitation damage in an Al alloy at temperatures between 500 and 550°C; they used a viscoplastic model based on a continuum mechanics framework for describing deformation and damage in this alloy. Riedel[14] has applied classical nucleation theory for cavity nucleation by stress concentration at second–phase particles during creep. Wang *et al.*[15] have employed classical nucleation theory and statistical methods to describe cavity nucleation in second–phase particles; cavity nucleation occurs from vacancy–supersaturated regions, creating a 'void phase' at the boundaries. They found that a critical stress concentration is needed for cavity nucleation to occur.

[1]Department of Materials Science and Metallurgy, University of Cambridge, 27 Charles Babbage Road, CB3 0FS Cambridge, UK
[2]Instituto de Investigaciones en Materiales, Universidad Nacional Autónoma de México PO Box 70-360, 04519 Mexico, DF, Mexico

*Corresponding author, email eg375@cam.ac.uk

** These limits are an estimate from experimental observations.

Published by Maney on behalf of the Institute
Received 2 May 2014; accepted 5 August 2014
DOI 10.1179/1743284714Y.0000000643

This concentration is determined mainly by the concentration and distribution of second–phase particles at grain boundaries. This model was applied to creep behaviour in Inconel MA 754. Borodin and Mayer[16] have proposed a mechanics-based model for resistance threshold of grain boundary sliding in nanocrystalline metals. The characteristic time of plastic relaxation due to grain boundary sliding is estimated from molecular dynamics simulation data. Zhou *et al.*[17] have proposed an energy approach to estimate crack initiation at triple junctions in nanocrystalline materials; at the steady state of initiation, the work done by the applied stress is dissipated by the grain–boundary rotational deformation, sliding and diffusion energies. This approach was applied to describe fracture toughness variations in materials with grains of sizes of 2–4 nm. Wang *et al.*[18] have proposed a similar energy-based model to investigate nanovoid nucleation in nanocrystalline materials; they have concluded that the nucleation mechanism is the result of grain boundary dislocations stopping at triple junctions during grain boundary sliding, causing stress increments and eventual cleavage. This work has been extended by Wang *et al.*[19] to describe nanovoid growth and coalescence by dislocation emission; they studied the crystal orientation effects on dislocation emission and the stress field increments around a nanovoid.

Modelling approaches for describing GBS–based superplastic behaviour are usually applied to a limited number of alloying systems and processing conditions. They employ phenomenological or semiempirical relations to link microstructural and deformation conditions, such as temperature and strain rate, thereby failing to provide further information on the superplastic response by modifying composition and deformation conditions. For instance, strain rate, grain size and temperature variations in superplastic alloys are usually described by a power–law relationship;[2] the exponents need to be identified for each alloy. Moreover, these expressions are not able to describe the alloy's flow stress evolution during straining.

The objective of this work is to present a thermodynamic approach, for describing flow stress evolution from grain boundary sliding in superplastic alloys. Grain boundary sliding is considered to be induced by dislocation intergranular movement. It is assumed that cavities are nucleated due to strain increments at grain boundaries causing grain boundary contact loss. The progress of cavities at grain boundaries (provoking material's softening and eventual failure) is obtained by describing the Gibbs free energy resulting from the competition between local stored and dissipation energy at moving boundaries; maximum superplastic flow can be achieved when both reach equilibrium.[6] The novelty of this work stems from applying thermostatistical principles to grain boundary sliding and cavity evolution: the entropy ΔS_{dis} describing the possible dislocation displacements (along a grain boundary) is employed to describe the energy loss of moving boundaries, reducing local stress concentrations. An evolution equation for the cavity density at grain boundaries is obtained from this analysis, describing the flow stress after reaching the ultimate tensile strength. This work is focused on describing GBS driven by intergranular dislocation movement.

The model is applied to describe superplastic behaviour of two Zn based alloys: Zn21Al2Cu and Zn22Al (wt-%), and a Mg alloy for different temperatures, strain rates, grain sizes, and specimen geometry. Cavity density and average radius are described for Zn22Al within the application range of the theory. Transition maps are defined to specify the optimal conditions for superplastic behaviour. It is shown how parameters such as deformation temperature and strain rate, chemical composition as well as microstructure, can be employed to tailor the superplastic response.

Experimental procedure

A Zn21Al2Cu[†] (wt-%) alloy was prepared by melting high purity Zn, Al, and Cu in an induction furnace. A 38 mm diameter cylindrical rod was obtained by continuous casting. The rod was cut, extruded at 563 K, and rolled at 513 K to obtain rolled bars of 2·54 mm thickness. Specimens for tensile testing with a gauge length of 6·35 mm were machined from the rolled sheets. The specimens then were solution treated at 623 K during 1 h and quenched in water at 288 K. A fine grained microstructure with an average grain size of 1 μm was obtained. Grain size measurements were performed by the mean intercept method. Tensile experiments were performed at a constant crosshead speed in a universal testing machine equipped with a thermostatic chamber. Specimens were deformed to fracture. Tensile tests were carried out at temperatures and strain rates in the range of $413 \leq T \leq 513$ K and $10^{-3} \leq \dot{\varepsilon} \leq 1\ s^{-1}$ respectively. Prior to deformation, the specimens were heated at 30°C min^{-1} and held during 20 min at the established testing temperature. A detailed description on the specimen's preparation and deformation procedures is shown in Ref. 20. True stress and (logarithmic) strains were measured in the tensile tests.

This is a strong Zn based alloy with yield strength of 400 MPa and a moderate density (5·4 g cm^{-3}). Below 550 K, this alloy shows a eutectoid microstructure composed of aluminium (α) and zinc (η) in solid solution, with small amounts of the intermetallic $CuZn_4$ (ε). Above 550 K, it shows a eutectic phase transformation. The high temperature phase (β) can be described as an aluminium FCC distorted structure.[21] The strength of Zinalco decreases with temperature, reaching a yield strength of 10 MPa at 530 K, and above 550 K the strength increases slightly (up to 25 MPa at 630 K).

Theory

Tensile deformation behaviour in superplastic alloys displays two regimes:[1]

(i) a hardening contribution due to grain boundary strengthening and/or dislocation accumulation. This proceeds upon reaching the ultimate tensile strength σ_{UTS} at an axial strain ε_{unif} (uniform elongation), where necking begins
(ii) a softening contribution, where grain boundary sliding mainly occurs ($\varepsilon > \varepsilon_{unif}$).

During this regime, local strain concentrations arise due to non-uniform boundary displacement causing contact loss between grains; cavity nucleation and coalescence takes place from this process with a concomitant stress reduction.[1,22] Although additional cavity nucleation can occur at grain boundaries (for instance, due to segregation of second–phase particles, carbides or impurities),

[†] Also, commercially referred to as Zinalco.

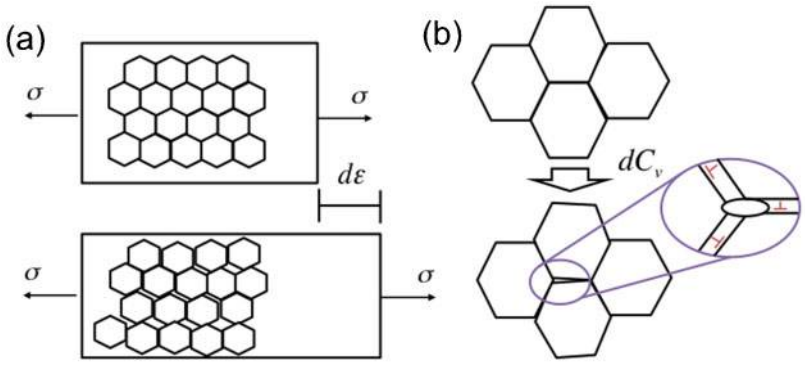

a collective displacement of several grains for strain increment $d\varepsilon$ and *b* cavity formation due to boundary displacement at grain–boundary level; intergranular dislocations are displayed in red

1 Schematic representation of system under consideration

this work is focused on describing cavity formation by intergranular sliding only, i.e. cavity formation at triple junctions. A cavity density at grain boundaries C_v can be defined as the number of cavities per unit area. The flow stress for $\varepsilon>\varepsilon_{unif}$, can then be approximated by the loss of the maximum strength (σ_{UTS}) due to cavity accumulation

$$\sigma_2 = \sigma_{UTS}\frac{C_v^0}{C_v} \tag{1}$$

where C_v^0 represents the initial cavity (areal) density ($\varepsilon=\varepsilon_{unif}$). The current analysis is performed in two dimensions (parallel and perpendicular to the tensile stress axis). Radial symmetry is assumed.[1] Figure 1 shows a schematic representation of (Fig. 1*a*) the collective displacement of several grains in the specimen for a strain increment $d\varepsilon$ at the macroscopic scale, and (Fig. 1*b*) cavity formation due to boundary displacement at the grain–boundary level. Grains of hexagonal shape are assumed. True (logarithmic) strains are considered in the model and in further calculations to be consistent with the experimental measurements. When considering several grains (Fig. 1*a*), if DC_v is the cavity density at the grain boundaries, where D is the average grain size, $DC_v d\varepsilon$ cavities form during $d\varepsilon$. On the other hand, at the grain boundary level (Fig. 1*b*), the cavity density increment dC_v is dictated by the boundary's ability to slide without cleavage.

For a strain increment $d\varepsilon$ in the specimen, the Gibbs free energy (per unit volume) to form a cavity (dG) depends on the competition between the strain energy build-up at the grain boundaries (dH), and the energy dissipation by grain boundary sliding (TdS)[6]

$$dG = dH - TdS \tag{2}$$

The latter term is related to dislocation motion, as grain boundary sliding is facilitated by the intergranular movement of dislocations within adjacent grains.[2] Similar to the work done by Onck and van der Giessen,[7] cavity behaviour is analysed at two (microscopic and macroscopic) levels. dG describes the energy increments due to cavity accumulation at the grain boundary level, whereas dH–TdS describes the energy variations as the strain increases in a region containing several grains. Equation (2) allows us to link the macroscopic stress/strain conditions (left hand side) with the microscopic events at the grain boundary level (right hand side). The energy balance is applied once the maximum tensile strength has been achieved, where it is assumed that the remaining 'strength' at higher strains is dictated by the material's affinity to accommodate strain increments via grain boundary sliding; it is assumed that the strain (including elastic) energy at this point has been converted into dislocations in the hardening stage; their ability to move at the grain boundaries dictates the rate at which the material's strength decreases.

At a grain boundary (microscopic) scale, dG is related to the grain boundary energy χ_{GB} around the additional number of cavities being formed.[23] The latter is approximated by the initial cavity length Λ_c, multiplied by the cavity density variation dC_v. Λ_c is considered to be a fraction of the average grain size $\Lambda_c=\beta_1 D$[‡], where D is the average grain size, and β_1 is a constant. dG becomes

$$dG = \chi_{GB}\frac{\beta_1}{2}DdC_v \tag{3}$$

where the 2 factor accounts for the shared effect of adjacent grains. It is worth noting that dC_v accounts for the cavity population variation with strain for a given temperature and strain rate.

At the macroscopic level, when several grains are considered, local strain increments at grain boundaries arise by grain boundary contact loss, leading to potential grain boundary cleavage and cavity formation.[25] dH is rationalised as the strain energy accumulation at the grain boundaries as the macroscopic strain increases ($d\varepsilon$). On the other hand, dislocation accumulation and pile-up activity at grain boundaries are significantly low in ultra fine grained materials than in their coarse-grained counterparts; strain hardening is virtually absent at $\varepsilon>\varepsilon_{unif}$, and dislocation generation is negligible.[3] Thus, it can be assumed that dislocation behaviour only features in grain-boundary accommodation via their motion and not by their accumulation; no strain energy due to dislocation activity is introduced. Additionally, it has been assumed that the strain energy has been converted into dislocations in the hardening stage, including the elastic energy. This implies that dH is only proportional to the grain boundary energy at $\varepsilon>\varepsilon_{unif}$; however this may not be the case if the hardening stage is also included in the energy balance. dH is approximated by (A) χ_{GB} for a cavity population

[‡] Although cavities display a preference to form at triple junctions, they can also be formed at any point of grain boundaries. For instance, Yin *et al.*[24] have observed cavity formation in other locations than triple junctions, during grain boundary sliding in Mg alloys.

variation on a given boundary $DC_v d\varepsilon$, (B) around the potential sites S_{sub} for cavity nucleation per grain. S_{sub} equals the grain perimeter per unit area[§]

$$S_{sub} = P_{grain} b / A_{grain}$$

where P_{grain} and A_{grain} are the perimeter and area of a grain respectively; S_{sub} is multiplied by b to approximate the atomic positions where cavities can nucleate, where b is the magnitude of the Burgers vector. For grains of hexagonal shape, it gives

$$S_{sub} = 3Db/(3 \times 3^{1/2}/8D^2) = 8b/(3^{1/2}D)$$

Also, (C) additional sites for cavity nucleation arise from the presence of other crystal defects at grain boundaries; this work considers solute atom effects only. The segregation of solute atoms at grain boundaries induces additional stress concentrations leading to additional cavity formation during subsequent deformation.[8,9,23,1] An additional term multiplying dH is included to account for solute effects; this term can be approximated by

$$1 + \frac{b}{\Lambda_{sol}}$$

where 1 incorporates pure material effects and b/Λ_{sol} accounts for solute segregation around the boundary,[26] Λ_{sol} is the solute atom mean spacing and equals $\Lambda_{sol} = b/x_{sol}^{1/3}$,[27] where x_{sol} is the solute atom fraction. Finally, dH equals

$$\begin{aligned} dH &= f_{geom} \underbrace{\chi_{GB} D C_v d\varepsilon}_{(A)} \underbrace{S_{sub}}_{(B)} \underbrace{(1 + x_{sol}^{1/3})}_{(C)} \\ &= \frac{8}{3^{1/2}} f_{geom} (1 + x_{sol}^{1/3}) b \chi_{GB} C_v d\varepsilon \end{aligned} \quad (4)$$

where f_{geom} is a geometric factor (proportionality constant) that depends on the specimen's shape. This factor is estimated in the section on 'Results'. It is worth noting that if second phase particles were included in the formulation, an additional term for particle mean free path may be present in (C).

Energy dissipation: dislocation entropy

It has been experimentally shown that GBS occurs through the movement of extrinsic dislocations along the boundaries.[2] This suggests the possibility of describing the energy dissipation by grain boundary sliding (TdS) in terms of dislocation behaviour. A statistical entropy ΔS_{dis} accounting for the energy dissipation due to the energetically favourable dislocation paths active during deformation has been proposed in previous work.[28,29] The number of possible dislocation path configurations increases as deformation evolves. Instead of trying to describe the instantaneous velocity gradient (or specific slide configurations), the entropy accounts for the total energy loss due to the different dislocation velocity configurations. ΔS_{dis} links the microscopic events of grain–boundary dislocation motion with the macroscopic strain rate.

The entropy is defined to account for the possible thermally activated dislocation migration paths when the applied stress is above the critical resolved shear stress and at constant macroscopic strain rates. A dislocation configuration is defined as the number of interatomic subunits a dislocation segment can glide during an arbitrary time step Δt.[28] At high temperatures, vacancy–dislocation interactions become dominant, increasing dislocation motion events via vacancy assisted climb and consequently additional configurations are incorporated.[30] The statistical entropy equals[26]

$$\Delta S_{dis} = k_B \ln\left(\frac{\dot{\varepsilon}_0}{\dot{\varepsilon}} + \frac{\vartheta}{\dot{\varepsilon}}\right) \quad (5)$$

where the first and second terms inside the logarithm argument account for the configurations due to pure dislocation slip and to vacancy–dislocation interactions respectively; $\dot{\varepsilon}_0 = cb\rho_Y$ is a limiting value for dislocation velocity (expressed as strain rate), a constant related to the speed of sound in the material, c; ρ_Y is the dislocation density consistent with the yield point [$\rho_Y = (\sigma_Y/0{\cdot}9\mu b)^2$ (Ref. 28)]; $\dot{\varepsilon}$ is the strain rate; b is the magnitude of the Burgers vector

$$\vartheta = \vartheta_D \exp\left(-\frac{E_m}{RT}\right)$$

is the vacancy migration frequency, wherein $\vartheta_D = 10^{13}\ s^{-1}$ is the Debye frequency, E_m is the vacancy migration energy, R is the gas constant and T is the absolute temperature. A detailed analysis and the derivation of the previous equations can be found elsewhere.[28,30] Note that as the strain rate tends to zero, ΔS_{dis} tends to infinity and becomes undefined; the energy balance in equation (2) is then no longer valid. This condition implies that the dislocation velocity is null and the number of possible dislocation paths is infinite, since their magnitude is null. Therefore, only constant, positive strain rates are currently considered in the model.

The differential entropy term in equation (2) is approximated by the statistical entropy (due to intergranular dislocation motion) per unit area $\frac{1}{bD} T\Delta S_{dis}$ for a cavity population variation $DC_v d\varepsilon$, where bD represents the area where intergranular dislocations can move

$$TdS = \frac{1}{Db} T\Delta S_{dis} D C_v d\varepsilon = \frac{1}{b} T\Delta S_{dis} C_v d\varepsilon \quad (6)$$

where the inclusion of C_v accounts for the number of cavities that are not formed due to stress relaxations (negative term in dG).[6] If dislocation activity at the grain boundaries is low, such as in the case of high strain rates, ΔS_{dis} is small, indicating that grain boundary sliding accommodation is inefficient and the cavity nucleation and growth increase. This is consistent with the conclusion outlined by Wang *et al.*[18] It is worth noting that all the experimental tests have been carried out at positive and constant strain rates, hence dS is only a function of ε. Although the strain rates can be different at the grain level, TdS aims in linking the macroscopic strain variations with the microscopic events at the grain level; a more detailed analysis of ΔS_{dis} is required if we would want to describe localised strain rate increments at triple junctions.

Combining equations (3), (4) and (6) the energy balance becomes

$$\begin{aligned} &\frac{\beta_1 D}{2} \chi_{GB} dC_v = \frac{8}{3^{1/2}} f_{geom} (1 + x_{sol}^{1/3}) b \chi_{GB} C_v d\varepsilon - \\ &\frac{1}{b} T\Delta S_{dis} C_v d\varepsilon \end{aligned} \quad (7)$$

[§] The current analysis is perfumed in two dimensions.

Rearranging the previous equation, the cavity evolution at grain boundaries becomes

$$\frac{dC_v}{d\varepsilon}=\frac{2b}{\beta_1 D}\left[\frac{8}{3^{1/2}}f_{geom}(1+x_{sol}^{1/3})-\frac{Tk_B\ln\left(\frac{\dot{\varepsilon}_0+\vartheta}{\dot{\varepsilon}}\right)}{\chi_{GB}b^2}\right]C_v$$
$$=\lambda_{GB}C_v \quad (8)$$

where

$$\lambda_{GB}=\frac{2b}{\beta_1 D}\left[\frac{8}{3^{1/2}}f_{geom}(1+x_{sol}^{1/3})-\frac{Tk_B\ln\left(\frac{\dot{\varepsilon}_0+\vartheta}{\dot{\varepsilon}}\right)}{\chi_{GB}b^2}\right] \quad (9)$$

is constant for a given strain rate and temperature. It is worth noting that λ_{GB} decreases if the temperature increases or the strain rate is reduced; if $\lambda_{GB}<0$, then it is fixed 0. Dividing by $d\varepsilon$ in equation 8 means estimating the microscopic cavity density variations with the macroscopic strain increments. The strain and time increments are equivalent, as constant macroscopic strain rates are considered ($\varepsilon=\dot{\varepsilon}t$); the cavity density increments with time are analogous to the density increments with strain under these conditions. A physical interpretation of $\lambda_{GB}=0$ is that the energy dissipation due to GBS (TdS) becomes higher than the formation energy for grain–boundary cavitation (dH); the flow stress evolution remains constant ($\sigma_2=\sigma_{UTS}$) as an efficient grain boundary motion (due to dislocation intergranular movement) dissipates stress concentrations in the material. This condition is further analysed in the section on 'Optimal conditions for superplastic behaviour'. Additional cavitation formation (and stress reduction) can occur at higher temperatures from other mechanisms, such as vacancy condensation at grain boundaries.[1]

Solving equation (8) and setting the initial condition $C_v=C_v^0$ at $\varepsilon=\varepsilon_{unif}$, the cavity density at grain boundaries becomes

$$C_v=C_v^0\exp[\lambda_{GB}(\varepsilon-\varepsilon_{unif})] \quad (10)$$

It is worth noting that the previous equation is defined for $\varepsilon>\varepsilon_{unif}$ only.

Zinalco and Zn22Al are eutectoid (HCP + FCC), and the analysis is modified to account for cavity behaviour on each phase: equation (2) is replaced by $dG=dG_{HCP}x_{HCP}+dG_{FCC}x_{FCC}$, where x_{HCP} and x_{FCC} are the atomic fractions of the HCP and FCC phases respectively; $dG_{HCP}=\frac{\beta_1 D}{2}\chi_{GB}^{HCP}d\rho_{GB}$ and $dG_{FCC}=\frac{\beta_1 D}{2}\chi_{GB}^{FCC}d\rho_{GB}$ are the free energies to nucleate a cavity in the HCP and FCC grain boundaries, respectively; χ_{GB}^{HCP} and χ_{GB}^{FCC} are the grain boundary energies of the HCP and FCC phase respectively. Similar modifications are made for equations (6) and (4) $dH=dH_{HCP}x_{HCP}+dH_{FCC}x_{FCC}$, with $dH_{HCP}=\frac{8}{3^{1/2}}f_{geom}(1+x_{sol}^{1/3})b_{HCP}\chi_{GB}^{HCP}\rho_{GB}d\varepsilon$ and $dH_{FCC}=\frac{8}{3^{1/2}}f_{geom}(1+x_{sol}^{1/3})b_{FCC}\chi_{GB}^{FCC}\rho_{GB}d\varepsilon$,*** where b_{HCP} and b_{FCC} are the magnitude of the Burgers vector of each phase; and $TdS=TdS_{HCP}x_{HCP}+TdS_{FCC}x_{FCC}$ with $TdS_{HCP}=\frac{1}{b_{HCP}}T\Delta S_{HCP}\rho_{GB}d\varepsilon$ and $TdS_{FCC}=\frac{1}{b_{FCC}}T\Delta S_{FCC}\rho_{GB}d\varepsilon$, where ΔS_{HCP} and ΔS_{FCC} are the entropy contributions of each phase. This modification alters the value of λ_{GB} only, but the solution of equation (8) is the same if the same grain size is considered for both phases. Mixed effects are ignored.

*** Solute effects are included in dH_{HCP} and dH_{FCC}, as cavities indistinctly form at grain boundaries of any phase.

Cavity radius

The cavity radius r evolves according to 1/3 the rate of the cavity density.[1,31] Thus, the differential equation describing cavity radius evolution becomes

$$\frac{dr}{d\varepsilon}=\frac{\lambda_{GB}}{3}r \quad (11)$$

Optimal conditions for superplastic behaviour

When $\lambda_{GB}=0$, strain accommodation by grain boundary sliding is maximum as it dissipates stress concentration effects, inducing the largest elongation range. A transition occurs from a flow stress instability (and sharp necking) produced by the accumulation of cavities around grain boundaries, to a diffuse necking produced by smooth boundary displacement with no stress reduction. Thus, optimal conditions for achieving superplastic deformation and a maximum elongation can be achieved. This is satisfied when the temperature, strain rate and solute composition follow the relation (equation (9))

$$\dot{\varepsilon}=(\dot{\varepsilon}_0+\vartheta)\exp\left[-\frac{8f_{geom}(1+x_{sol}^{1/3})\chi_{GB}b^2}{3^{1/2}k_BT}\right] \quad (12)$$

This equation defines the limits for superplastic forming for achieving maximum elongation.

Results

The present model is compared with the new data presented here for Zn21Al2Cu, and with experimental data from the literature for Zn22Al and Mg3Al1Zn (wt-%). The flow stress evolution ($\varepsilon>\varepsilon_{unif}$) is obtained from equations (1) and (10). Table 1 shows the chemical composition of each alloy.

Concurrent cavitation can interrupt superplastic deformation to cause premature failure by the cavity percolation in the direction perpendicular to the tensile axis.[1] Sharp surfaces induce premature failure, as voids and cracks may form at the specimen's edges.[1] Thus, a geometry factor f_{geom} (equation (9)) is defined for comparing the specimen characteristic cross-section length l_{spec} (diameter or thickness for circular or squared sections, respectively) with an equivalent diameter ϕ_{eq} of the same area, if the specimen would have circular shape

$$\phi_{eq}=2\left(\frac{A_{spec}}{\pi}\right)^{1/2} \quad (13)$$

Table 1 Tested alloys

Alloy/wt-%	Authors	Geometry	l_{spec}/mm	A_{spec}/mm^2	f_{geom}
Zn21Al2Cu	This study	Squared	2·54	6·45	1·12
Zn22Al	Ref. 38	Cilindrical	6	28·3	1
Zn22Al	Ref. 39	Cilindrical	4	12·5	1
Zn22Al	Ref. 44	Squared	2·54	6·45	1·12
Mg3Al1Zn	Ref. 40	Rectangular	6(2)	12	0·77
Mg3Al1Zn	Ref. 41	Cilindrical	6	28·3	1
Mg3Al1Zn	Ref. 42	Squared	5	25	1·12

Table 2 Physical parameters

Metal	b/nm	c/m s^{-1}	E_m/eV	χ_{GB}/J m^{-2}	μ/GPa
Zn	0·268	3850	0·5	0·350	47·3exp[−0·003(T−273)]
Al	0·286	5000	0·57	0·325	29·4–0·015T
Cu	0·256	3810	…	0·625	47·4exp(−0·0039T)
Mg	0·32	4940	0·7	0·640	18·53–0·0045T−8·7 × 10^{-6}T^2

where A_{spec} is the specimen's cross-sectional area. f_{geom} is defined to introduce additional cavity formation when the specimen's geometry contains sharp corners since the specimen is assumed of cylindrical shape; this parameter accounts for cavity formation at these locations since this work is based on a mean field approach. For the case of specimens with rectangular shape, l_{spec} is approximated by an equivalent diameter of a specimen with circular cross-section and the same perimeter. The geometry factor becomes

$$f_{geom} = \frac{l_{spec}}{\phi_{eq}} \tag{14}$$

Table 1 shows the values of l_{spec}, ϕ_{eq} and f_{geom} for a number of experimental configurations reported in the literature. It is worth noting that this factor depends on the specimen's geometry only.

In order to obtain the physical input parameters for modelling each alloy, a mixture rule is used for b, χ_{GB}, c and μ[26,32]

$$P = (1 - \sum_i x_i) P_{(1-\sum_i x_i)} + \sum_i x_i P_{x_i}$$

where P_{x_i} and x_i represent the physical parameter and composition values of the ith element[††] respectively. For the Zn21Al2Cu alloy, it was confirmed with Thermocalc that Al and Cu are initially contained in the FCC phase and Zn in the HCP phase. Table 2 shows the values of the physical parameters of pure materials; they were obtained from the literature, except for the grain boundary energy of Mg; this value was fitted as no published information was found. b, c, E_m and χ_{GB} values were obtained from[33,34] and[35] respectively; μ for Zn was obtained from,[36] Al and Cu from,[28] and Mg from.[37] For the Zn22Al2Cu alloy, E_m in the FCC phase was taken equal to the migration energy in pure Al, whereas for Mg3Al1Zn, E_m was taken equal to the energy in pure Mg. β_1=0·0005 was taken for all alloys.

Similar to Cu in Zn21Al2Cu, the presence of Al and Zn atoms in the Mg3Al1Zn alloy contribute to the solute effects in equation (4); for this case $x_{sol}^{1/3} = x_{Al}^{1/3} + x_{Zn}^{1/3}$ is considered.[‡‡] Figure 2 shows the experimental values employed for (a) σ_{UTS} and (b) ε_{unif} at different conditions; the horizontal axis is expressed in terms of the parameter $DT\ln(10^7/\dot{\varepsilon})$, where 10^7 s^{-1} is a reference strain rate; this parameter merges temperature, strain rate and grain size variations into a single axis. These values were directly obtained from the experimental stress–strain curves. σ_{UTS} was employed instead of σ_Y to estimate $\dot{\varepsilon}_0$ (equation (5)), as in most cases necking occurs at low strains and σ_{UTS} and σ_Y are of the same order. It was also assumed for Zinalco and Zn22Al that $\sigma_Y = \sigma_Y^{HCP} x_{HCP} + \sigma_Y^{FCC} x_{FCC}$. This simple rule is employed as the ρ_Y term (including σ_Y effects) in equation (5) is part of the logarithm argument, hence no substantial variations in the model are expected.

Figure 3 shows the model and experimental results for Zn21Al2Cu alloy deformed at different temperatures, strain rates and strains up to 1. The model shows good agreement with respect to the experiments. However, it shows a higher softening rate at higher strain rates above 5×10^{-2} s^{-1}; this discrepancy can be due to the model predicting smaller effects from dislocation intergranular movement, preventing efficient grain boundary accommodation and a subsequent strength loss. λ_{GB}=0 occurs at 513 K and 10^{-3} s^{-1}; the model predicts that these are the optimal conditions for superplastic flow and no sharp necking occurs. This was experimentally confirmed in previous work by Ramos Azpeitia *et al.*[20]

Figure 4 shows the model results and their comparison with experimentally obtained curves for Zn22Al[38,39] at different temperatures, strain rates and grain sizes. The model shows good agreement in all cases, except at 373 K, 10^{-1} s^{-1} and D=1·3 μm, and at 303 K, 10^{-3} s^{-1} and D=0·9 μm; the model shows a lower softening rate with respect to the experimental data. This discrepancy can be due to early fracture development.

Figure 5 shows the model results and their comparison with experiments at different temperatures, strain rates and grain sizes for a Mg3Al1Zn alloy. The experimental data were obtained from Refs. 40–42. The model shows good agreement for all tested conditions.

The average cavity radius and density are compared against experimental results for a Zn22Al alloy; they were obtained from Ref. 43. Measurements of cavity number and size were made directly by optical microscopy. The initial conditions were set to match the first experimental measurement (ε_0=0·2). Figure 6 shows the model predictions for the (a) average cavity radius and (b) number of cavities per square millimetre at different temperatures, and strain rates with D=1·3 μm and its comparison with experimental results. The initial cavity radii at 303 and 473 K were assumed 0·24 and 0·34 μm respectively, whereas for the initial cavity density at 303 and 473 K were 4200 and 485 cavities mm^{-2} respectively. The model shows good results for the average radius and density at 303 K; however, at 473 K the model does not predict cavity evolution as λ_{GB}=0. As pointed out by Nieh *et al.*,[1] the limiting factor for tensile ductility is the intergranular cavity interaction on the direction perpendicular to the tensile axis; nevertheless, additional cavity generation in other directions and grain interiors occurs. The model describes the cavity behaviour along the specimen's cross-section only. Also, additional cavity formation may occur from other mechanisms not being considered in this work.

Figure 7 shows the transition maps for the optimal conditions for superplastic deformation for (a) Zn22Al

[††] Weighted contributions are computed expressing x_i in atom fraction

[‡‡] The solute segregation around a boundary equals

$$\frac{b}{\Lambda_{sol}} = \frac{b}{\Lambda_{sol}^{Al}} + \frac{b}{\Lambda_{sol}^{Zn}} = x_{Al}^{1/3} + x_{Zn}^{1/3}.$$

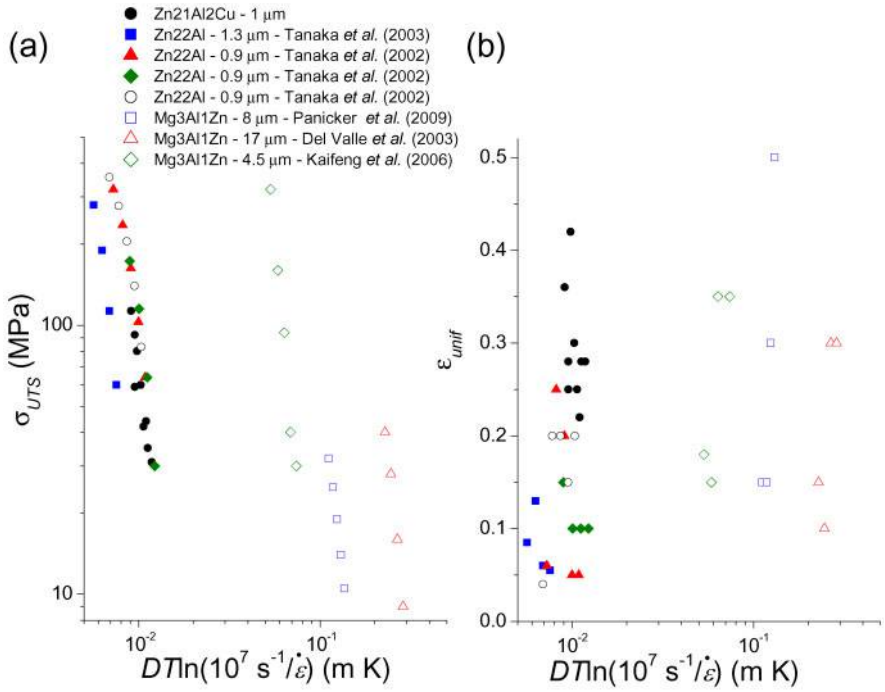

2 Experimental values for *a* σ_{UTS} and *b* ε_{unif} employed in model

and (b) Zn21Al2Cu, and their comparison with experimental data. For Zn22Al, the data were obtained from Ref. 44; the experimental points show the range when maximum elongation occurs. For Zn21Al2Cu, the red squares show the conditions where sharp necking occurred, and the blue dots show the conditions where a diffuse neck was observed. A detailed analysis of the specimen's final form can be found in Ref. 20. The shadowed areas show the superplastic region; maximum elongation conditions occur in the transition lines between the white and shadowed areas. The model shows good agreement for Zn21Al2Cu, whereas for Zn22Al it predicts a difference in the transition temperature of ~20 K below the experimental measurements. The superplastic regions outline the conditions where optimal elongation can occur, although an additional criterion based on the true plastic strain for failure should be assessed.

To illustrate the use of this theory for determining the optimal superplastic forming and maximum elongations conditions, Fig. 7*c* shows the superplastic flow instability variation for different solid solution (Cu) concentrations in a Zn21Al alloy. The model shows an increase of ~30, ~60, and ~75°C in the optimal superplastic flow conditions if 0·1, 1 and 2 wt-% of copper are added to the alloy respectively. The model shows that, although

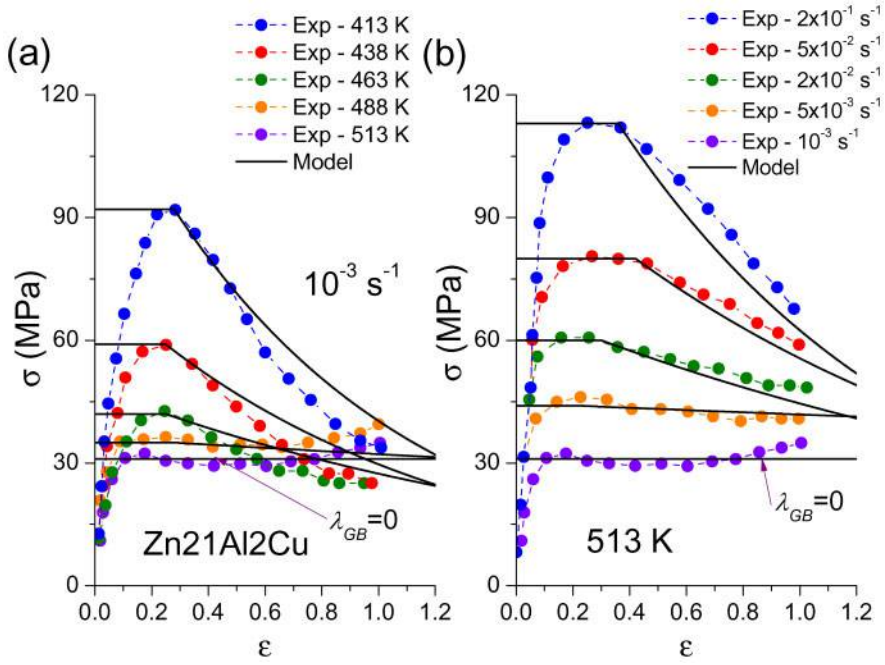

3 Flow stress evolution of Zn21Al2Cu with grain size of 1 μm for different *a* temperatures and *b* strain rates

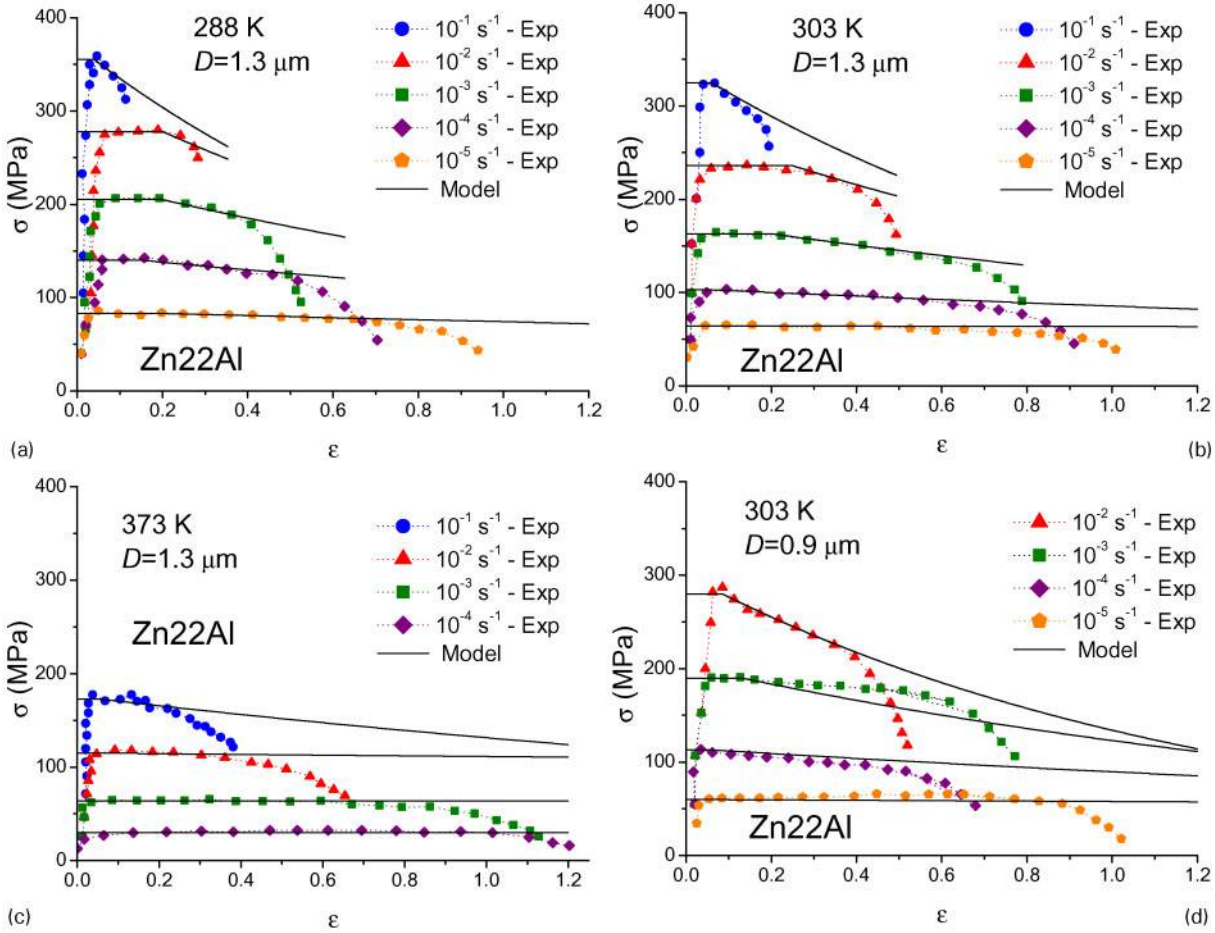

4 Flow stress evolution of Zn22Al for different temperatures, strain rates and grain sizes: experimental data obtained from Refs. 38 and 39

solid solution increases the alloy's strength, it also increases the temperature or decreases the strain rate for achieving optimal superplastic flow. This is experimentally verified in Fig. 7*a* and *b*, when an increase of 2% of copper (Zinalco) and a reduction of 1% of aluminium (Zn22Al) shows an increase in the optimal conditions of ~65°C.

Discussion

Aimed at the design and improvement of superplastic alloys, a new model to describe cavity formation at grain boundaries from grain boundary sliding (driven by dislocation motion) has been presented. The Gibbs free energy dG for cavity formation is proposed to equal the competition between the stored energy at grain boundaries dH and the dissipation from sliding boundaries TdS. The latter is proportional to the dislocation entropy ΔS_{dis} which accounts for the energy loss from moving dislocations, facilitating boundary migration. dG is obtained by performing a local analysis on the cavity population variation dC_v at grain boundaries, whereas dH and TdS are obtained by considering cavity effects, in a number of grains, during a strain increment $d\varepsilon$. dH includes additional formation effects from the specimen's geometry and solute segregation at grain boundaries.

A differential equation describing the cavity density at grain boundaries with strain is obtained and the flow stress evolution after the ultimate tensile strength is predicted. The constant λ_{GB} (equation (9)) describes the material's dependence on the composition and processing conditions. $T\Delta S_{dis}$ controls the temperature and strain rate dependance of λ_{GB}. When $\lambda_{GB}=0$, a transition from sharp necking failure to superplastic flow stress instability occurs; this allows to map the optimal conditions for superplastic deformation.

The model is tested via describing the flow stress evolution for three alloys (two Zn- and one Mg-based) and for wide temperature, strain rate, composition, grain size and specimen's geometry ranges. Additionally, the cavity density C_v and average radius r evolution with strain are also described for Zn22Al at deformation conditions where $\lambda_{GB} \geq 0$. Only one parameter was adjusted ($\beta_1=0{\cdot}0005$), and remained constant for all alloys and deformation conditions. Good agreement is achieved for single (Mg) and dual (Zn) phase alloys, although interfacial effects have been neglected. Further effects may be considered in future work.

This analysis remains valid for cavity evolution below the optimal conditions to achieve superplastic flow instability, where cavity accumulation occurs mostly at grain boundaries and GBS is driven by dislocation movement. Extensions to describe cavitation kinetics above these conditions can be made in future work. Although vacancy behaviour is considered through the entropy term (incorporating the possible vacancy configurations), additional terms may be needed in the free energy for cavity nucleation (equation (3)) to account for vacancy supersaturation at grain boundaries. The effect of second phase particles can also be introduced in

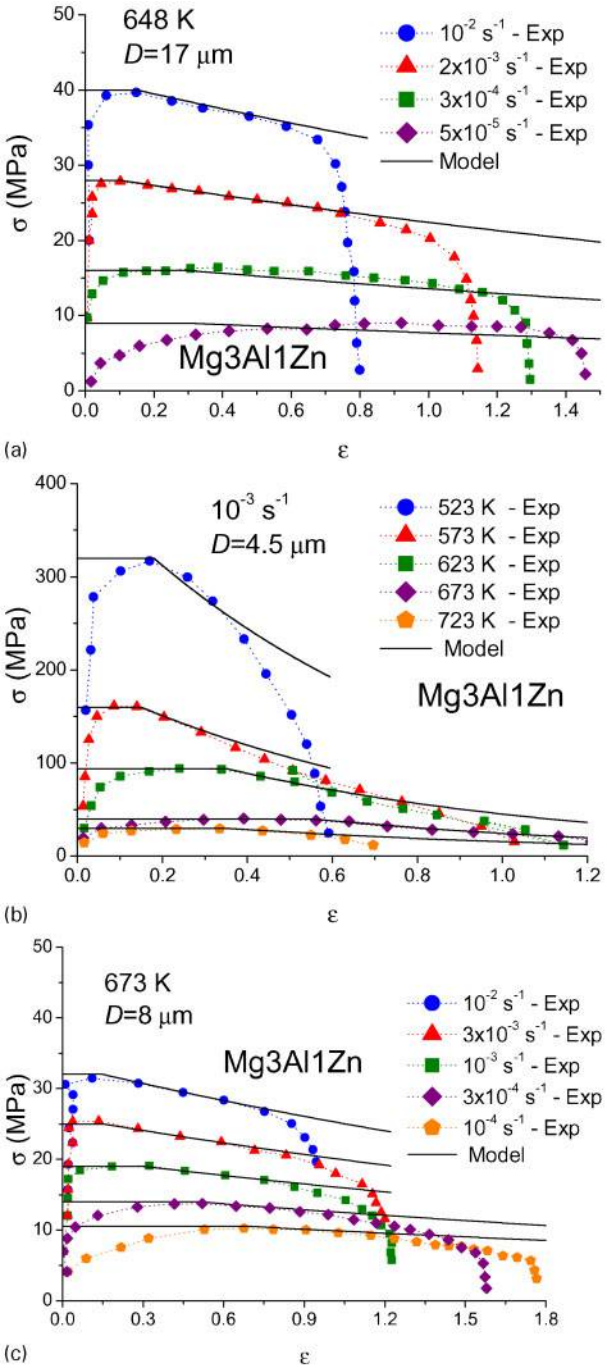

5 Flow stress evolution of Mg3Al1Zn with different grain sizes *a* at 648 K and different strain rates, *b* different temperatures and at 10^{-3} s^{-1}, and *c* at 673 K and different strain rates: experimental data were obtained from Refs. 40–42.

the formulation by including an additional term in the cavity nucleation free energy.

Constant and positive strain rates only were considered in the model. As pointed out above, if the strain rate is null, the entropy is undefined and the current analysis will no longer be valid. A similar case occurs if variable strain rates are considered: the entropy also changes in time, modifying the energy expressions and the overall formulation, such as considering time increments dt instead of strain increments $d\varepsilon$ in equation (8). This is important in describing the maximum elongation for failure, since localised void and crack formation and propagation require local and variable strain rates to be considered at the grain level. This suggests a need to revisit some of the terms involved in the entropy formulation to account for null and variable strain rates, an aspect to be explored in future work.

The dislocation entropy concept is applied to describe the energy dissipation of dislocations moving along grain boundaries in the Gibbs free energy; they facilitate and dictate the grain boundary sliding rate, preventing further cavity formation. Moreover, this formulation has been employed in a number of plasticity phenomena where dislocations feature:

(i) a thermodynamic analysis on an annihilating dislocation segment is employed to determine the dynamic recovery rate and work hardening during straining.[29] From this analysis, the transitions from low, medium and high temperature dislocation annihilation mechanisms have been analytically obtained[30]

(ii) the entropy also features in the description of dislocation cell formation and evolution in metals:[45] a thermodynamic balance between a dislocation forest and cellular arrangements has been performed, where $T\Delta S_{dis}$ describes the energy dissipation of dislocations moving in the material to form cells

(iii) this approach has also been applied to describe the energy barrier for grain growth during dynamic recrystallisation,[26] with entropy accounting for the energy loss due to grain boundary motion (acting as a driving force for grain growth). With this approximation, the use of the grain boundary mobility concept can be circumvented, and mobility fitting parameters are not required.[26]

Transition maps for superplastic instability provide a theoretical tool to find the optimal processing conditions when new alloys are designed, incorporating solid solution effects. Further extensions can be made for other systems where intermetallic or precipitate particles are present, such as in Ti, Al and Ni based alloys to describe their optimal processing conditions.[1] This work can aid in better understanding cavity nucleation during superplastic deformation at various strain rates, by introducing grain–boundary dislocation activity effects in the entropy term. Nevertheless, further work is needed to fully unravel localised cavity nucleation, as this work only covers the overall mechanical behaviour of superplastic alloys.

The current approach can also be used as an input to other modelling techniques such as the finite element method to describe spatial evolution of sliding grains and shape variation in a given specimen. The mathematical model remains valid once the ultimate tensile strength has been reached, and it does not describe grain boundary strengthening effects prior to this point. Also, a criterion for failure and to predict total elongation is missing. The model may also be extended to describe grain boundary sliding and cavity nucleation under creep conditions by modifying ΔS_{dis} and incorporating the relevant dislocation kinetics relations in equation (5). These extensions will be tackled in future.

Conclusions

A new thermostatistical theory describing superplastic behaviour and cavity evolution of alloys has been presented. A thermodynamic analysis on the free energy

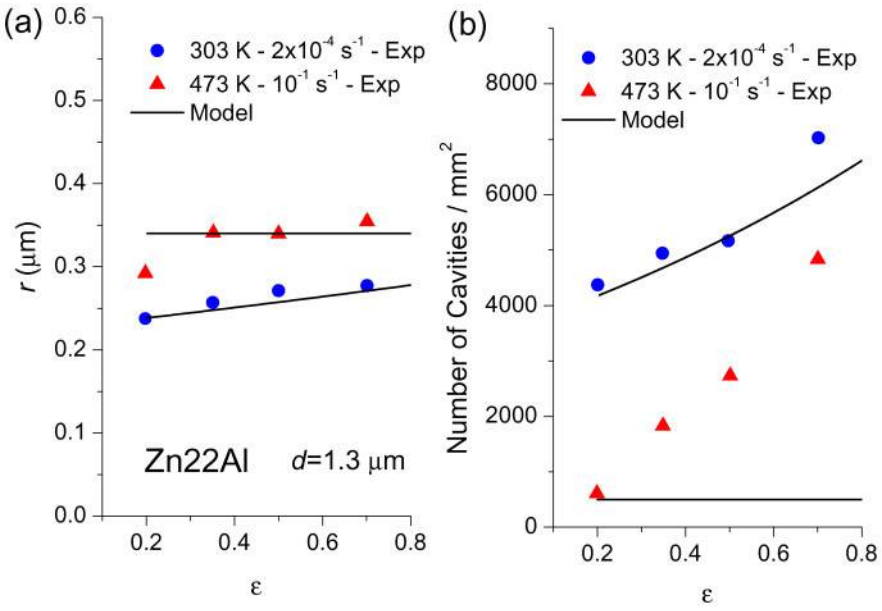

6 Evolution of *a* average cavity radius and *b* number of cavities for different deformation conditions for Zn22Al: experimental data obtained from Ref. 43

for cavity nucleation at the boundaries has been performed to describe their evolution. The theory is able to prescribe the flow stress, cavity density and average radius evolution at strains above the uniform elongation at various temperatures, strain rates, grain sizes, and specimen geometries. The model was successfully applied to Zn22Al, Zn21Al2Cu and Mg3Al1Zn. Transition maps were obtained for finding the optimal conditions for superplastic behaviour in terms of composition, temperature and strain rate. The effect of copper in a Zn21Al alloy was examined, demonstrating the capacity of this approach for designing new superplastic alloys.

It was also demonstrated that the dislocation entropy plays a major role in superplastic behaviour, as it relates the energy loss due to migrating boundaries with the strain rate. This term allows us to postulate the free energy value for cavity nucleation due to grain boundary

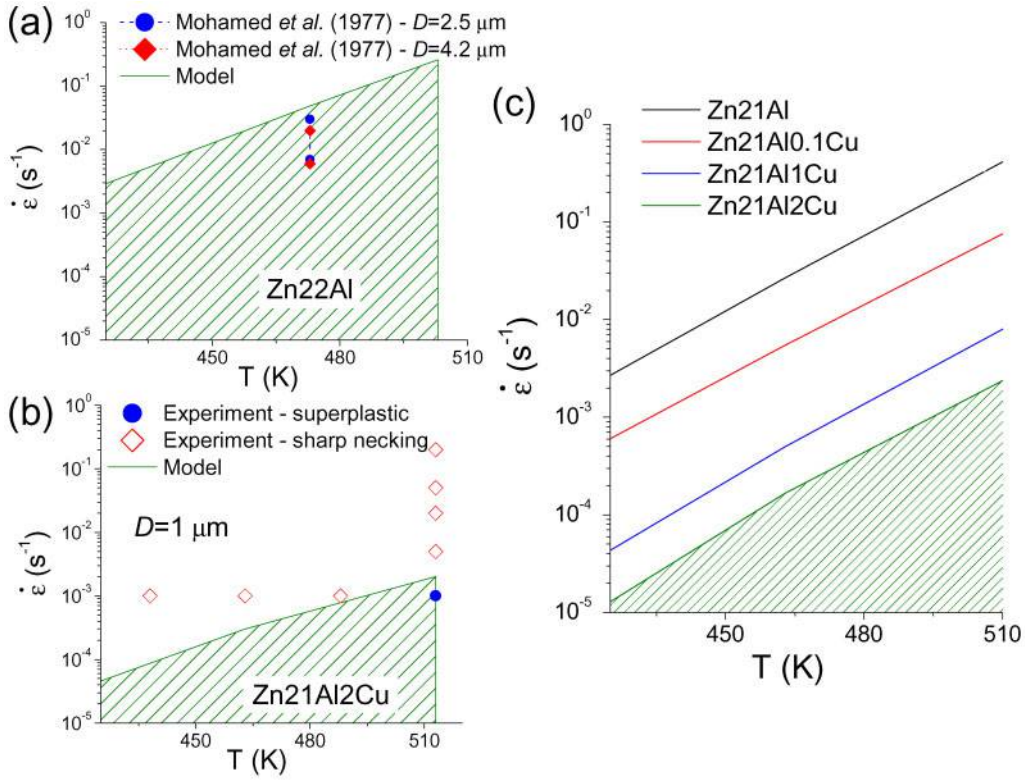

7 Transition maps for superplastic flow instability and maximum elongation occurs for *a* Zn22Al, *b* Zn21Al2Cu and *c* different solid solution (copper) concentration: experimental data in *a* were obtained from Ref. 44; shadowed areas show superplastic region; maximum elongation conditions occur in transition lines between white and shadowed areas

sliding at different processing conditions, allowing to optimise the associated processing schedules.

Acknowledgements

E. I. Galindo-Nava is grateful to the National Council of Science and Technology of Mexico (CONACYT) via the program 'Becas para estudios de posgrado en el extranjero' and the Roberto Rocca Education Program for the provision of financial support.

References

1. T. G. Nieh, J. Wadsworth and O. D. Sherby: 'Superplasticity in metals and ceramics'; 2005, Cambridge, Cambridge University Press.
2. T. G. Langdon: 'Grain boundary sliding revisited: Developments in sliding over four decades', *J. Mater. Sci.*, 2006, **41**, 597–609.
3. M. A. Meyers, A. Mishra and D. J. Benson: 'Mechanical properties of nanocrystalline materials', *Prog. Mater. Sci.*, 2006, **51**, 427–556.
4. H. Van Swygenhoven, M. Spaczer and A. Caro: 'Microscopic description of plasticity in computer generated metallic nanophase samples: A comparison between Cu and Ni', *Acta Mater.*, 1999, **47**, 3117–3126.
5. H. Van Swygenhoven and P. M. Derlet: 'Grain–boundary sliding in nanocrystalline fcc metals', *Phys. Rev. B*, 2001, 224105.
6. R. J. DiMelfi: 'Grain boundary sliding and its relation to ductility and fracture in fine–grained polycrystalline materials with a particular focus on γ-TiAl', *Mater. Sci. Eng. A*, 1997, **A237**, 141–149.
7. P. Onck and E. van der Giessen: 'Growth of an initially sharp crack by grain boundary cavitation', *J. Mech. Phys. Solids*, 1999, **47**, 99–139.
8. M. A. Khaleel, H. M. Zbib and E. A. Nyberg: 'Constitutive modelling of deformation and damage in superplastic materials', *Int. J. Plas.*, 2001, **17**, 277–296.
9. M. E. Kassner and T. A. Hayes: 'Creep cavitation in metals', *Int. J. Plas.*, 2003, **19**, 1715–1748.
10. H. Toda, Z. A. B. Shamsudin, K. Shimizu, K. Uesugi, A. Takeuchi, Y. Suzuki, M. Nakazawa, Y. Aoki and M. Kobayashi: 'Cavitation during high–temperature deformation in Al–Mg alloys', *Acta Mater.*, 2013, **61**, 2403–2413.
11. Y. Qi and P. E. Krajewski: 'Molecular dynamics simulations of grain boundary sliding: The effect of stress and boundary misorientation', *Acta Mater.*, 2007, **55**, 1555–1563.
12. B. N. Kim, K. Hiraga and K. Morita: 'Viscous grain–boundary sliding and grain rotation accommodated by grain–boundary diffusion', *Acta Mater.*, 2005, **53**, 1791–1798.
13. B. N. Kim, K. Hiraga, K. Morita, H. Yoshida and B. W. Ahn: 'Viscous grain–boundary sliding with rotating particles or grains', *Acta Mater.*, 2009, **57**, 5730–5738.
14. H. Riedel: 'Cavity nucleation at particles on sliding grain boundaries A shear crack model for grain boundary sliding in creeping polycrystals', *Acta Metall.*, 1984, **32**, 313–321.
15. J. S. Wang, J. J. Stephens and W. D. Nix: 'A statistical analysis of cavity nucleation at particles in grain boundaries', *Acta Metall.*, 1985, **33**, 1009–1021.
16. E. N. Borodin and A. E. Mayer: 'A simple mechanical model for grain boundary sliding in nanocrystalline metals', *Mater. Sci. Eng. A*, 2012, **A532**, 245–248.
17. J. Zhou, L. Hu, H. Liu and M. Hu: 'An energy approach to account for crack initiation in nanocrystalline materials', *Mater. Design*, 2013, **52**, 30–35.
18. L. Wang, J. Zhou, S. Zhang, Y. Liu and S. Dong: 'Effects of accommodated grain boundary sliding on triple junction nanovoid nucleation in nanocrystalline materials', *Mech. Mater.*, 2014, **71**, 10–20.
19. L. Wang, J. Zhou, D. Hui and S. Zhang: 'Micromechanics model of nanovoid growth and coalescence by dislocation emission: loading and lattice orientation effects', *Int. J. Mech. Sci.*, 2014, **79**, 168–175.
20. M. Ramos Azpeitia, E. E. Martínez Flores and G. Torres Villaseñor: 'Superplastic behaviour of Zn–Al eutectoid alloy with 2% Cu', *J. Mater. Sci.*, 2012, **47**, 6206–6212.
21. A. Sandoval-Jiménez, J. Negre and G. Torres Villaseñor: 'The triclinic high temperature modification of the α phase of the Zn–Al system', *Mater. Res. Bull.*, 1999, **34**, 2291–2296.
22. A. H. Chokshi: 'Cavity nucleation and growth in superplasticity', *Mater. Sci. Eng. A*, 2005, **A410**, 95–99.
23. X. G. Jiang, J. C. Earthman and F. A. Mohamed: 'Cavitation and cavity–induced fracture during superplastic deformation', *J. Mater. Sci.*, 1994, **29**, 5499–5514.
24. D. L. Yin, K. F. Zhang, G. F. Wang and W. B. Han: 'Superplasticity and cavitation in AZ31 Mg alloy at elevated temperatures', *Mater. Lett.*, 2005, **59**, 1714–1718.
25. J. Intrater and E. S. Machlin: 'Grain boundary sliding and inter crystalline cracking', *Acta Metall.*, 1959, **7**, 140–143.
26. E. I. Galindo-Nava and P. E. J. Rivera-Díaz-del-Castillo: 'Thermostatistical modelling of hot deformation in FCC metals', *Int. J. Plas.*, 2013, **47**, 202–221.
27. D. Hull and D. J. Bacon: 'Introduction to dislocations', Butterworth-Heineman, 1999.
28. E. I. Galindo-Nava, J. Sietsma and P. E. J. Rivera-Díaz-del-Castillo: 'Dislocation annihilation in plastic deformation: II kocks-mecking analysis', *Acta Mater.*, 2012, **60**, 2615–2624.
29. E. I. Galindo-Nava and P. E. J. Rivera-Díaz-del-Castillo: 'Modelling multiscale plasticity: a thermostatistical approach', *Scr. Mater.*, 2012, **67**, 915–918.
30. E. I. Galindo-Nava and P. E. J. Rivera-Díaz-del-Castillo: 'A thermostatistical theory of low and high temperature deformation in metals', *Mater. Sci. Eng. A*, 2012, **A543**, 110–116.
31. M. J. Stowell, D. W. Livesey and N. Ridley: 'Cavity coalescence in superplastic deformation', *Acta Metall.*, 1984, **32**, 35–42.
32. I. Toda-Caraballo, E. I. Galindo-Nava and P. E. J. Rivera-Díaz-del-Castillo: 'Unravelling the materials genome: symmetry relationships in alloy properties', *J. Alloy Compd*, 2013, **566**, 217–228.
33. D. R. Lide: 'CRC handbook of chemistry and physics', CRC Press, 2008.
34. R. Cahn and P. Haasen: 'Physical metallurgy', North Holland, 1996.
35. J. Hirth and J. Lothe: 'Theory of dislocations', Wiley Interscience Publication, 1982.
36. J. P. Andrews: 'The variation of Young's modulus at high temperatures', *Proc. Phys. Soc. London*, 1924, **37**, 169–177.
37. E. I. Galindo-Nava and P. E. J. Rivera-Díaz-del-Castillo: 'Thermostastitical modelling of deformation twinning in HCP metals', *Int. J. Plas.*, 2014, **55**, 25–42.
38. T. Tanaka, K. Makii, A. Kushibe and K. Higashi: 'Room temperature deformation behaviour of Zn-22 mass%Al alloy with nano crystalline structure', *Mater. Trans.*, 2002, **43**, 2449–2454.
39. T. Tanaka, K. Makii, A. Kushibe and K. Higashi: 'Capability of superplastic forming in the seismic device using Zn–22Al eutectoid', *Scripta Mater.*, 2003, **49**, 361–366.
40. R. Panicker, A. H. Chokshi, R. K. Mishra, R. Verma and P. E. Krajewski: 'Microstructural evolution and grain boundary sliding in a superplastic magnesium AZ31 alloy', *Acta Mater.*, 2009, **57**, 3683–3693.
41. J. A. Del-Valle, M. T. Perez-Prado and O. A. Ruano: 'Deformation mechanisms responsible for the high ductility in a Mg AZ31 alloy analyzed by electron backscattered diffraction', *Metall. Mater. Trans. A*, 2005, **36A**, 1427–1438.
42. Z. Kaifeng, Y. Deliang, W. Guofeng and H. Wenbo: 'Superplastic deformation behavior of hot–rolled AZ31 magnesium alloy sheet at elevated temperatures', *J. Wuhan Univ. Technol.*, 2006, **21**, 1–6.
43. T. Tanaka, Y. Takigawa and K. Higashi: 'Effect of temperature on the cavity nucleation rate for fine–grained Zn–22 wt% Al alloy', *Scr. Mater.*, 2008, **58**, 643–646.
44. F. A. Mohamed, M. M. Ahmed and T. G. Langdon: 'Factors influencing ductility in the superplastic Zn22Al eutectoid', *Metall. Trans. A*, 1977, **543A**, 933–938.
45. E. I. Galindo-Nava and P. E. J. Rivera-Díaz-del-Castillo: 'A thermodynamic theory for dislocation cell formation in FCC metals', *Acta Mater.*, 2012, **60**, 4370–4378.